

Dynamically Stable and Intimately Bonded Li/Garnet Interface for High-Areal-Capacity Solid-State Lithium-Metal Batteries

Jintao Liu, Xiayueyang Mei, Jie Wang, Sisir Pokhrel, and Hailei Zhao*

A multifunctional $\text{Li}_3\text{N}-\text{Li}_2\text{O}$ hybrid interlayer is elaborately designed and constructed by a facile one-step surface etching method to address the issues of lithium dendrite penetration and the interfacial Kirkendall voids formation in solid-state lithium metal batteries based on garnet-type electrolyte

$\text{Li}_{6.4}\text{La}_3\text{Zr}_{1.4}\text{Ta}_{0.6}\text{O}_{12}$. The constructed $\text{Li}_3\text{N}-\text{Li}_2\text{O}$ hybrid interlayer greatly promotes interfacial lithium-ion conduction while dramatically reducing leakage of electronic current from the lithium anode to garnet by three orders of magnitude. Most importantly, the introduced $\text{Li}_3\text{N}-\text{Li}_2\text{O}$ interlayer shows a high interfacial work of adhesion with both garnet and Li, preventing detachment between the lithium metal and electrolytes during the lithium stripping process, even at high areal capacity cycling. Benefiting from such a synergistic effect, the assembled lithium symmetric cell exhibits a high critical current density of 2.6 mA cm^{-2} and achieves a stable cycling for over 100 h for an ultrahigh areal capacity of 4.0 mAh cm^{-2} at a current density of 0.4 mA cm^{-2} .

due to its relatively high ionic conductivity ($10^{-4}\text{--}10^{-3} \text{ S cm}^{-1}$), wide electrochemical window (0–5 V), high mechanical strength ($\approx 60 \text{ GPa}$ of shear modulus), and excellent chemical stability against lithium metal.^[6,7] However, garnet-based SSLMBs still suffer from the inevitable lithium dendrite penetration under a high-rate cycling condition and severe Kirkendall voids formation between the Li anode and SSEs after high-areal-capacity cycling, which collectively hinder their commercial applications.^[8–15]

The lithium dendrite propagation issue, which is primarily attributed to the poor SSEs-LMA contact and the undesirable electron leakage from lithium metal to LLZTO electrolyte, will result in internal short-circuiting and pose safety concerns for battery operation.^[9,10] Conquering the dendrite issue in garnet-based SSLMBs necessitates simultaneous optimization of Li/LLZTO

interfacial contact and suppression of electron leakage from the lithium anode to SSEs.^[16–23] Several strategies have been proposed to achieve intimate Li/LLZTO contact. One effective strategy is removing the spontaneously generated lithiophobic Li_2CO_3 passivation layer on the surface of LLZTO by scratching the electrolyte with sandpapers in argon atmosphere, and subsequently coating the LLZTO surface with certain metals (Au, Ag, Al, W, Bi, etc.), which can in situ alloy with melting lithium metal to form a tightly bonded Li/SSEs connection, by magnetron sputtering or atomic layer deposition.^[3,11,24–29] Although these introduced metallic interlayers can promote uniform and rapid lithium-ion conduction, thereby inhibiting interfacial lithium dendrite propagation, they are typically electron conductors, fail to block the electron injection from the lithium bulk, allowing lithium dendrites to still potentially nucleate inside the LLZTO electrolyte during cycling.

Recent studies have increasingly focused on using metal halides (ZnF_2 , AlF_3 , BiCl_3 , etc.), to improve interfacial adhesion through reactive wetting between lithium metal and metal compounds, while forming an electronically insulating layer (LiF , LiCl , etc.).^[30–32] These constructed bifunctional interlayers can reduce the interfacial resistance to some extent while maintaining exceptionally high electronic insulation ($<10^{-10} \text{ S cm}^{-1}$), which collectively leads to the fundamental suppression of lithium dendrite growth in SSLMBs. Nevertheless, the formation of interfacial voids, driven by the kinetically-limited mass transport

1. Introduction

Lithium metal anode, possessing an exceptional theoretical specific capacity of 3860 mAh g^{-1} and the most negative redox potential of -3.04 V versus the standard hydrogen electrode, has long been recognized as the ultimate anode material.^[1–3] Solid-state lithium metal batteries (SSLMBs), employing mechanically rigid solid-state electrolyte (SSEs), are promising in enabling the safe utilization of lithium metal anode, thereby achieving next-generation electric vehicle batteries with both high energy density and excellent safety performance.^[4,5] Among various SSEs, cubic garnet-type LLZTO ($\text{Li}_{6.4}\text{La}_3\text{Zr}_{1.4}\text{Ta}_{0.6}\text{O}_{12}$), as a representative oxide electrolyte, has attracted extensive attention

J. Liu, X. Mei, J. Wang, S. Pokhrel, H. Zhao
School of Material Science and Engineering
University of Science and Technology Beijing
Beijing 100083, P. R. China
E-mail: hlzhao@ustb.edu.cn

J. Wang, H. Zhao
Beijing Municipal Key Laboratory of New Energy Materials and Technologies
Beijing 100083, P. R. China

 The ORCID identification number(s) for the author(s) of this article can be found under <https://doi.org/10.1002/adfm.202512943>

DOI: [10.1002/adfm.202512943](https://doi.org/10.1002/adfm.202512943)

of Li atoms necessary to compensate for Li dissolution into LLZTO, remains unresolved during high-areal-capacity cycling, leading to contact loss and irreversibly enhancing polarization voltage, eventually triggering premature battery failure.^[11,13–15] Applying an external stack pressure exceeding 2 MPa to the battery can mitigate the interfacial voids formation issue, thereby enabling stable long-term cycling with an areal capacity above 1.0 mAh cm⁻².^[15,33,34] However, the utilization of significant load pressure increases the complexity and operational cost of the battery, which is unfavorable for its practical application. Therefore, it is imperative to develop an effective interlayer between lithium metal and garnet electrolyte, which should simultaneously promote the interfacial lithium-ion conduction, inhibit the leakage of electrons from the lithium anode to electrolytes, and most importantly, achieve a dynamically stable and intimate Li/SSEs contact without void formation even after high-areal-capacity cycling.

Herein, a multifunctional hybrid interlayer was established between Li and LLZTO through a facile one-step surface etching method. In the design process of etching-acid selection, two critical limitations must be considered: 1) the lithophilic/lithiophobic nature of reaction products derived from the selected acid and the Li₂CO₃ coating layer, which would affect the intimate contact with Li metal anode; 2) the lithium-ion conductivity of the intermediate layer, which is essential to ensure a fast lithium-ion transport across the interface between Li and LLZTO. Based on above two considerations and thermodynamic feasibility calculations (as show in Note S1, Supporting Information), nitric acid was selected to convert the Li₂CO₃ lithiophobic layer on LLZTO surface into a LiNO₃ layer, which can spontaneously in situ react with molten Li to form a Li₃N-Li₂O hybrid interlayer, resulting in a tightly-bonded Li/SSEs connection. The generated high-bandgap Li₂O serves as an electron insulator, effectively blocking electron leakage from Li into LLZTO, while the highly lithium-ion conductive Li₃N nanoparticles uniformly dispersed in Li₂O matrix facilitate homogeneous Li ion diffusion across the interface. Such a strategy reduces the interfacial impedance from 35 to 6 Ω cm² at room temperature while substantially reduces the leakage electron current from 5.91 × 10⁻⁹ to 6.95 × 10⁻¹² A cm⁻² when tested at an applied external voltage of 1.0 V. Most importantly, the composite interfacial interlayer shows a high work of adhesion with both garnet and Li as demonstrated by density functional theory calculations, so that the detachment will not occur during lithium stripping process even after a high-areal-capacity cycling. As a result, the assembled lithium symmetric cell exhibits a high critical current density of 2.6 mA cm⁻² and achieves a stable cycling for over 100 h for an ultra-high areal capacity of 4.0 mAh cm⁻² at current density of 0.4 mA cm⁻². Besides, the fabricated full cells using LiFePO₄ as cathode show an excellent long-term stability and deliver a reversible discharge capacity of 150.1 mAh g⁻¹ after 250 charge-discharge cycles at 0.5C.

2. Results and Discussion

Solid state electrolyte Li_{6.4}La₃Zr_{1.4}Ta_{0.6}O₁₂ (LLZTO) with a relative density of ≈95% and an ionic conductivity of 4.8 ± 0.1 × 10⁻⁴ S cm⁻¹ (25 °C) was prepared by the conventional solid-state method (Figure S1, Supporting Information). After

storing in air for 2 h, the LLZTO pellet was etched with nitric acid for 30 s (LLZTO-N30), which results in a coating layer on the surface of the LLZTO-N30 sample (Figure S2, Supporting Information). The X-ray diffraction (XRD) pattern of pristine LLZTO sample shows sharp and well-defined peaks corresponding to cubic garnet type LLZTO (PDF#45-0109, Figure 1a), while besides the main cubic garnet structure, additional peaks at 24.8° and 42.4° are detected from LLZTO-N30 sample, which demonstrates the formation of LiNO₃ (PDF#80-0203). Raman spectra were used to identify the surface components of the LLZTO and LLZTO-N30 samples (Figure 1b). For the pristine LLZTO sample, peaks at 1053 cm⁻¹ corresponding to Li₂CO₃ are observed. After treating with HNO₃, the peak due to Li₂CO₃ disappears, and the characteristic peak of LiNO₃ (1083 cm⁻¹) is identified. X-ray Photoelectron Spectroscopy (XPS) characterization was conducted to further investigate surface compositions of the pristine LLZTO and LLZTO-N30 pellets. As shown in Figure 1c, the C 1s spectrum of LLZTO contains peaks corresponding to the O=C=O (289.9 eV), C=O (288.5 eV), and C–O bonds (286.1 eV), suggesting the presence of a Li₂CO₃ layer on the LLZTO surface.^[18] Differently, the LLZTO-N30 sample shows a dramatic reduction in intensity of all Li₂CO₃-related peaks in C 1s spectrum, and displays a prominent peak corresponding to LiNO₃ at 407.6 eV in N 1s spectrum (Figure S3, Supporting Information), demonstrating that LiNO₃ is formed in situ on the LLZTO surface via the spontaneous reaction between Li₂CO₃ and HNO₃ (Table S1, Supporting Information).^[35,36]

The existence and distribution of LiNO₃ are further revealed by scanning electron microscope (SEM) and energy-dispersive spectroscopy (EDS). The EDS mapping clearly shows an abundance of C elements present on the surface of the pristine LLZTO sample, revealing the existence of a Li₂CO₃ coating layer (Figure 1d). The cross-sectional SEM image and the corresponding EDS line-scanning results of the LLZTO clearly reveal the existence of a Li₂CO₃ layer, with a thickness of ≈200 nm, uniformly coating on the surface of LLZTO (Figure S4, Supporting Information). After acid treatment, the surface of LLZTO is uniformly composed of the N element, with negligible C element, demonstrating the transformation of surface Li₂CO₃ to LiNO₃ (Figure 1e). LLZTO samples with nitric acid treatment for different times (10, 30, 120 s) demonstrate significant time-dependent surface morphology (Figure S5, Supporting Information). Specifically, after 10 s of HNO₃ treatment, the coated Li₂CO₃ gradually disappears and LiNO₃ begins to appear. With 30 s of acid etching, the surface Li₂CO₃ is completely transformed into a uniformly distributed LiNO₃ layer. However, after etching the electrolyte with HNO₃ for 120 s, the surface of LLZTO grains reveals an irregular mesh-like morphology, which is attributed to the acid-induced structural degradation. The distribution and the thickness of the generated LiNO₃ interlayers were investigated. For the LLZTO-N30 pellet, no obvious surface morphology deterioration is observed, and the LiNO₃ interlayer with a thickness of ≈5 μm is tightly adhered to the surface of LLZTO (Figure S6, Supporting Information).

The modified electrolyte demonstrates substantially enhanced wettability with lithium metal, characterized by a reduction in the wetting angle from 128° to 43°, which can be attributed to the spontaneous reaction between Li and LiNO₃, as supported by the thermodynamic calculation (Figure S7 and Table S1, Supporting Information). Benefiting from the enhanced wettability, molten

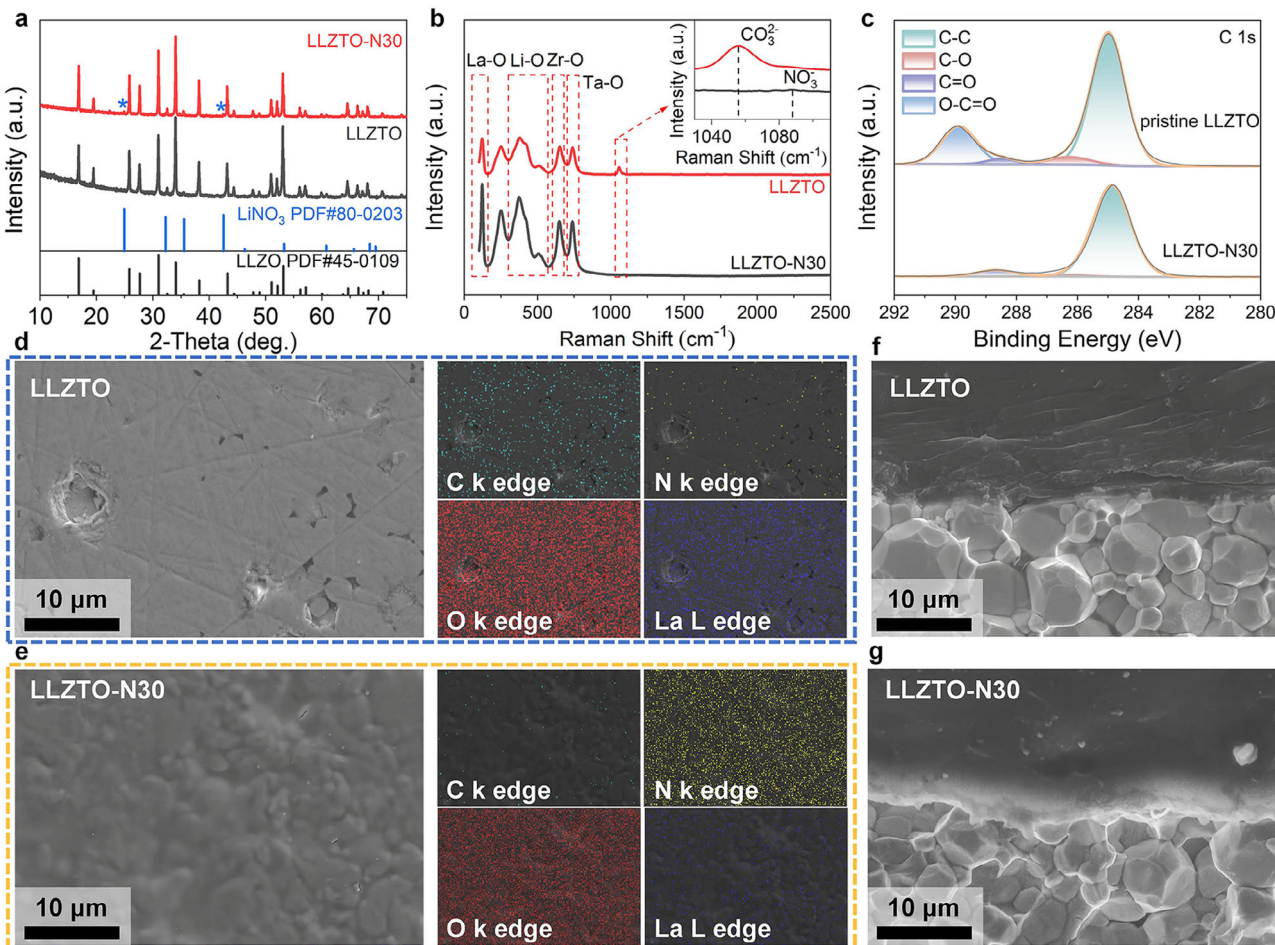


Figure 1. XRD patterns (a) and Raman spectra (b) of LLZTO and LLZTO-N30 pellets. XPS spectra of C 1s of LLZTO and LLZTO-N30 pellets (c). Surface SEM images and corresponding EDS elemental mapping images of LLZTO (d) and LLZTO-N30 (e). Cross-sectional SEM images of Li/LLZTO interface (a) and Li/LLZTO-N30 interface (b).

lithium can spread completely and uniformly on the surface of the LLZTO-N30 pellet, whereas the unmodified electrolyte shows poor adhesion with molten lithium at 250 °C, rendering it unable for lithium symmetric cells assembly (Figure S8, Supporting Information). To address this limitation, intimate Li/SSEs contacts were achieved in all the prepared symmetric cells by immersing the electrolytes in molten lithium metal at a raised temperature of 350 °C (Figure 1f,g; Figure S9, Supporting Information).

EDS line-scanning results clearly reveal the presence of a thin interlayer (<1 μm), rich in O and N, between the Li and LLZTO-N30 interface (Figure 2a). To precisely identify the specific composition of this intermediate interlayer, the coating of lithium metal on the LLZTO surface was removed by an electrochemical stripping procedure. Specifically, the Li|LLZTO-N30|Li symmetric cell was charged persistently at a current density of 0.1 mA cm⁻² for 80 h (8 mAh cm⁻²) to completely strip the lithium. After that, an electrolyte with a purplish-red surface layer was obtained (Figure S10, Supporting Information). The cross-sectional SEM image and EDS mapping clearly show the presence of an O-rich and N-rich coating layer on the LLZTO-N30 surface, which corresponds to the generated Li₂O and Li₃N, as

demonstrated by the XRD results (Figure 2b,c). These results confirm that molten lithium can react spontaneously with LiNO₃ to form a Li₃N-Li₂O hybrid intermediate layer, which is consistent with the thermodynamic calculation results (Table S1, Supporting Information).

To investigate the impact of the constructed Li₃N-Li₂O hybrid layer on interfacial lithium-ion conduction, electrochemical impedance spectroscopy (EIS) of the constructed Li symmetric cells was collected at room temperature (~25 °C), and a significantly reduced interfacial resistance from ~35 to ~6 Ω cm² was observed for the assembled Li|LLZTO-N30|Li symmetric cell (Figure 2d). The interfacial impedance of lithium symmetric cells was further tested at different temperatures (0, 35, 50, 65, and 80 °C) to calculate the activation energy (E_a) of lithium-ion transportation across the Li/Garnet interface according to the Arrhenius equation (Figure S11 and Table S2, Supporting Information). Notably, the E_a of lithium-ion transportation across Li/LLZTO-N30 interface reduces from 0.45 to 0.39 eV, indicating a facilitated interfacial lithium-ion conduction, which is attributed to the transformation of the lithium-ion insulating Li₂CO₃ (σ_{Li^+} : 10⁻¹⁵ S cm⁻¹ at 25 °C)^[37] passivation layer to

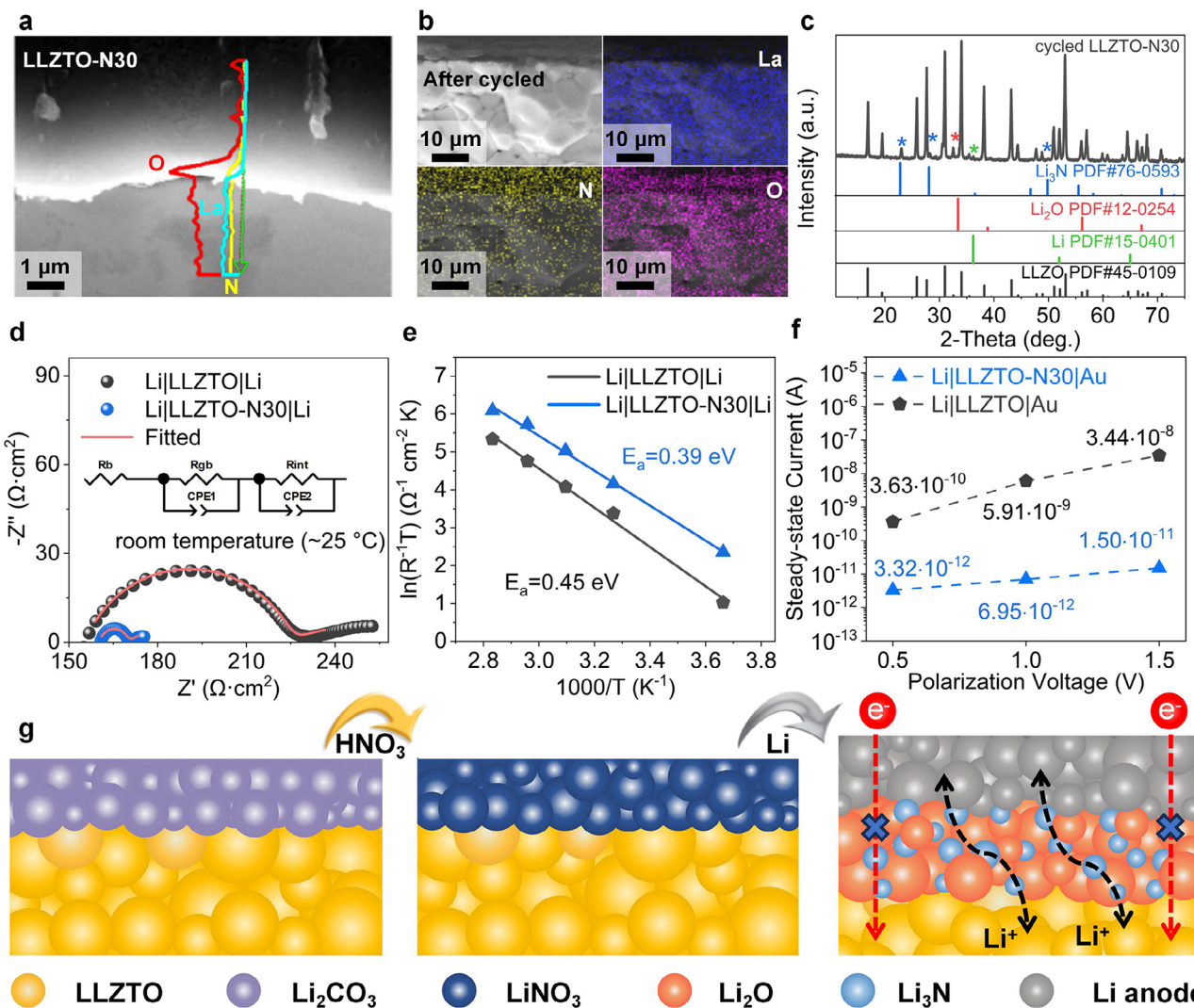


Figure 2. Cross-sectional SEM images with corresponding EDS line scanning profile/mapping images of $\text{Li}|\text{LLZTO-N30}$ interface before cycling (a), and after electrochemical stripping procedure (b). XRD pattern of the surface of LLZTO-N30 after electrochemical stripping (c). EIS data with fitting results of $\text{Li}|\text{LLZTO}| \text{Li}$ and $\text{Li}|\text{LLZTO-N30}| \text{Li}$ symmetric cells at room temperature (~25 °C) (d). Comparison of interfacial lithium-ion transportation activation energy of Li/Garnet interfaces (e). Steady-state current values of Hebb–Wagner cells under different applied external voltages (f). Schematic illustration of in situ conversion reaction constructed multifunctional hybrid interlayer (g).

$\text{Li}_3\text{N}-\text{Li}_2\text{O}$ (σ_{Li^+} : 10^{-3} and 10^{-12} S cm $^{-1}$ at 25 °C, respectively)^[38,39] hybrid lithium-ion conducting layer (Figure 2e). The well-improved interfacial lithium-ion conduction is beneficial for enabling homogeneous Li plating/stripping.

To investigate the electron-blocking effect of the $\text{Li}_2\text{O}-\text{Li}_3\text{N}$ layer, Hebb-Wagner cells with gold coated on one side and lithium coated on the opposite side of the SSEs ($\text{Li}|\text{SSEs}| \text{Au}$ cell) were constructed and subsequently tested by the chronoamperometry method. The obtained steady-state currents can be nearly considered as the leakage electron current of the Hebb-Wagner cells under different biases. Notably, the $\text{Li}|\text{LLZTO-N30}| \text{Au}$ cell displays an obviously reduced steady-state current compared with the $\text{Li}|\text{LLZTO}| \text{Au}$ cell under all the applied external voltages (Figure 2f). Specifically, the leakage current of the $\text{Li}|\text{LLZTO-N30}| \text{Au}$ cell significantly decreases from 5.91×10^{-10} to 6.95×10^{-12} A cm $^{-2}$ when tested at a bias of 1.0 V, demon-

strating that the injection of electrons from lithium bulk to the electrolyte is effectively impeded by the constructed $\text{Li}_2\text{O}-\text{Li}_3\text{N}$ interlayer (Note S2 and Figure S12, Supporting Information). To elucidate the mechanism by which the introduced $\text{Li}_2\text{O}-\text{Li}_3\text{N}$ interlayer impedes electron tunneling from Li metal into LLZTO bulk, density functional theory (DFT) calculations were carried out to determine the bandgaps of the Li_2O and Li_3N . Although Li_3N exhibits a bandgap of merely 1.06 eV, Li_2O , which is three times the amount of Li_3N (Table S1, Supporting Information), features a wide bandgap of 4.94 eV (Figure S13, Supporting Information), substantially wider than that of LLZTO (~4.0 eV).^[40] The wide bandgap Li_2O serves as an electron insulator, preventing electron leakage from Li into LLZTO, while the highly lithium-ion conductive Li_3N nanoparticles, well-dispersed in Li_2O matrix, enable uniform Li ion diffusion through the interface, which is believed to be beneficial

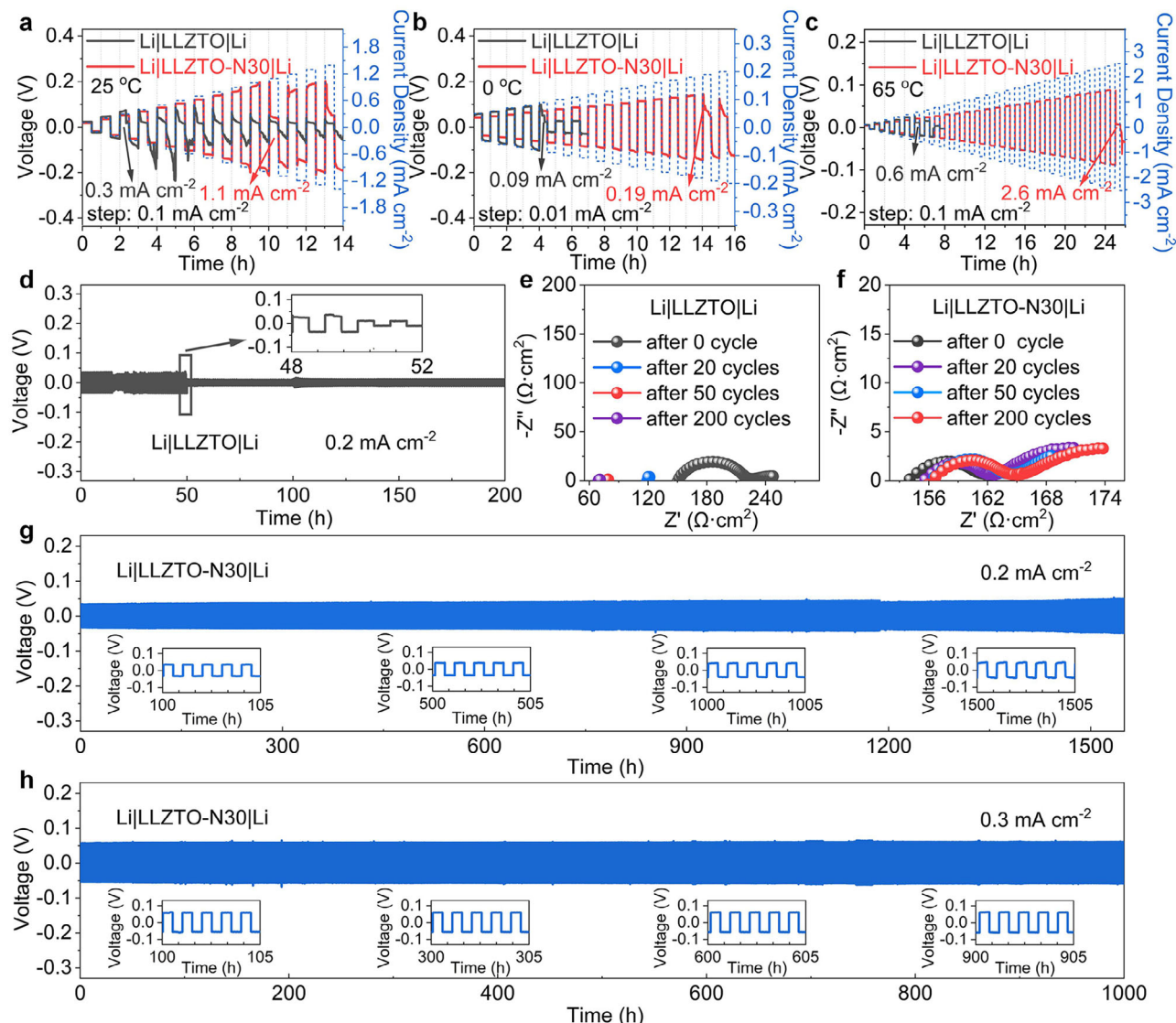


Figure 3. CCD of $\text{Li}|\text{LLZTO}| \text{Li}$ and $\text{Li}|\text{LLZTO-N30}| \text{Li}$ symmetric cells at 25°C (a), 0°C (b), and 65°C (c). Prolonged galvanostatic cycling performance of $\text{Li}|\text{LLZTO}| \text{Li}$ (d) under 0.2 mA cm^{-2} at 25°C . Comparison of EIS plots of $\text{Li}|\text{LLZTO}| \text{Li}$ (e) and $\text{Li}|\text{LLZTO-N30}| \text{Li}$ (f) symmetric cells after cycling at 0.2 mA cm^{-2} for 0, 20, 50, 200 cycles. Prolonged galvanostatic cycling performance of $\text{Li}|\text{LLZTO-N30}| \text{Li}$ cells under 0.2 mA cm^{-2} (g), and 0.3 mA cm^{-2} at 25°C (h).

for suppressing lithium dendrite growth during battery cycling (Figure 2g).

To demonstrate the beneficial effect of $\text{Li}_2\text{O}-\text{Li}_3\text{N}$ interlayer in suppressing lithium dendrites penetration, the critical current density (CCD) of the assembled lithium symmetric cells ($\text{Li}|\text{LLZTO}| \text{Li}$, $\text{Li}|\text{LLZTO-N10}| \text{Li}$, and $\text{Li}|\text{LLZTO-N30}| \text{Li}$) was tested. For the $\text{Li}|\text{LLZTO}| \text{Li}$ cell, a CCD of merely 0.3 mA cm^{-2} is observed when tested at 25°C (Figure 3a). Notably, the $\text{Li}|\text{LLZTO-N10}| \text{Li}$ cell shows a CCD of 0.9 mA cm^{-2} , slightly lower than that of the $\text{Li}|\text{LLZTO-N30}| \text{Li}$ cell (1.1 mA cm^{-2}) (Figure 3a; Figure S14, Supporting Information). This is related to the still-existing lithium carbonate layer on the LLZTO-N10 surface, which impedes lithium-ion conduction, as indicated by the interfacial impedance results (Figure S15, Supporting Information). The significant improvement in CCD of $\text{Li}|\text{LLZTO-N30}| \text{Li}$ cell is at-

tributed to the complete transformation from the surface Li_2CO_3 layer to a $\text{Li}_2\text{O}-\text{Li}_3\text{N}$ hybrid layer, which substantially promotes interfacial lithium-ion conduction, while simultaneously serving as an electron insulation layer, blocking the potential electron leakage from lithium metal, and eventually inhibiting the growth of lithium dendrites. Thanks to such a synergistic effect, the $\text{Li}|\text{LLZTO-N30}| \text{Li}$ cell delivers an increased CCD from 0.09 to 0.19 mA cm^{-2} , and an increased CCD from 0.6 to 2.6 mA cm^{-2} at 0 and 65°C , respectively, which further confirms the advantages of the hybrid layer in suppressing dendrite growth in a wide temperature range. (Figure 3b,c).

The benefits of the established interlayer are further evaluated by comparing the long-term stability of lithium symmetric cells. At a current density of 0.2 mA cm^{-2} (0.1 mAh cm^{-2}), the $\text{Li}|\text{LLZTO}| \text{Li}$ shows a large overpotential of $\approx 40 \text{ mV}$, which drops

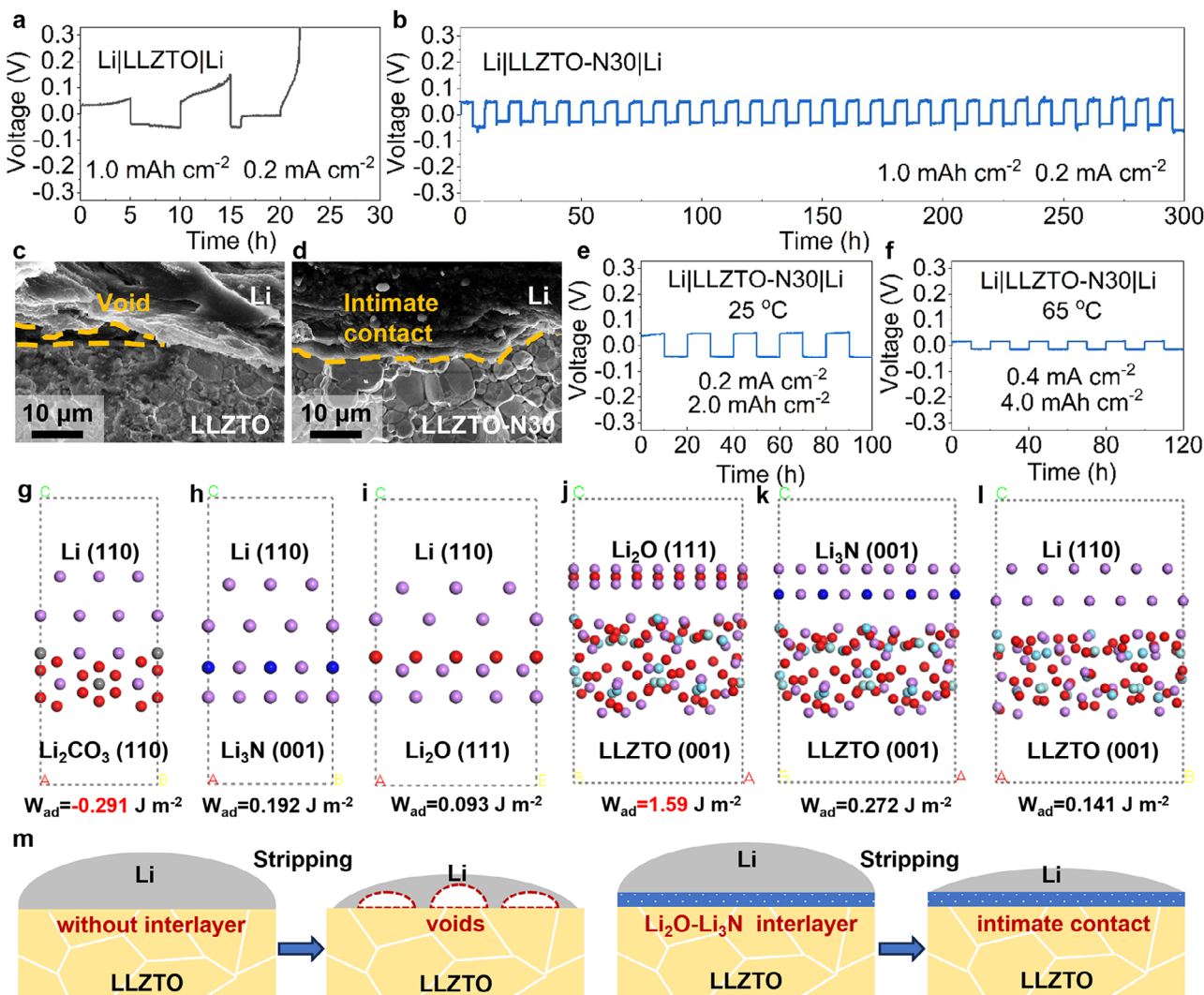


Figure 4. Galvanostatic cycling test of $\text{Li}|\text{LLZTO}|\text{Li}$ (a) and $\text{Li}|\text{LLZTO-N30}|\text{Li}$ (b) symmetric cells at 1.0 mAh cm^{-2} . Cross-sectional SEM images of $\text{Li}|\text{LLZTO}$ (c) and $\text{Li}|\text{LLZTO-N30}$ (d) interfaces after cycling at 1.0 mAh cm^{-2} . Galvanostatic cycling test of $\text{Li}|\text{LLZTO-N30}|\text{Li}$ symmetric cells at 2.0 mAh cm^{-2} (e), and 4.0 mAh cm^{-2} (f). Atomic structures and corresponding W_{ad} of $\text{Li}/\text{Li}_2\text{CO}_3$ (g), $\text{Li}/\text{Li}_3\text{N}$ (h), $\text{Li}/\text{Li}_2\text{O}$ (i), $\text{Li}_2\text{O}/\text{LLZTO}$ (j), $\text{Li}_3\text{N}/\text{LLZTO}$ (k), and Li/LLZTO interfaces (l). Schematic illustration of the evolution of the Li/Garnet interfaces during the lithium anode stripping process (m).

sharply after merely 50 cycles and is accompanied by a persistent decrease in both ohmic and interfacial resistances during cycling, indicating a severe short circuit happening (Figure 3d,e). After disassembling the short-circuited $\text{Li}|\text{LLZTO}|\text{Li}$ cells, a severe lithium dendrite penetration was clearly observed by SEM (Figure S16, Supporting Information). In comparison, due to the partial removal of Li_2CO_3 and generation of $\text{Li}_3\text{N}-\text{Li}_2\text{O}$, a stable cycling of 1000 h is achieved in $\text{Li}|\text{LLZTO-N30}|\text{Li}$ cell (Figure S17, Supporting Information). Notably, $\text{Li}|\text{LLZTO-N30}|\text{Li}$ cell can be cycled stably with a low overpotential of $\approx 30 \text{ mV}$ for more than 1500 h at a current density of 0.2 mA cm^{-2} (Figure 3g). The nearly unchanged ohmic and interfacial impedance, and the non-detection of lithium dendrite, indicate the excellent stability of the $\text{Li}|\text{LLZTO-N30}|\text{Li}$ cells (Figure 3f; Figure S16, Supporting Information). In addition, the $\text{Li}|\text{LLZTO-N30}|\text{Li}$ cells achieve stable cycling for over 1000 h even at a higher current density of

0.3 mA cm^{-2} (Figure 3h). The ultra-long cycling stability confirms that the established hybrid interlayer significantly enhances the resistance of the battery to lithium dendrite formation, enabling dendrite-free SSLMBs.

To evaluate the impact of the constructed interlayer on maintaining a dynamically stable intimate Li/SSEs contact, galvanostatic cycling experiments were carried out for an increased areal capacity of 1.0 at 0.2 mA cm^{-2} . A large voltage polarization occurs when the $\text{Li}|\text{LLZTO}|\text{Li}$ cell is cycled for only 15 h, whereas the $\text{Li}|\text{LLZTO-N30}|\text{Li}$ cell is cycled stably for over 300 h with stable polarization voltage (Figure 4a,b). For the $\text{Li}|\text{LLZTO}|\text{Li}$ cell, the $\text{Li}|\text{LLZTO}$ interface severely detaches after the deep lithium stripping process (Figure 4c), resulting in the large voltage polarization. In sharp contrast, a dynamically stable intimate-contact $\text{Li}|\text{LLZTO-N30}$ interface is observed after cycling at 1 mAh cm^{-2} for

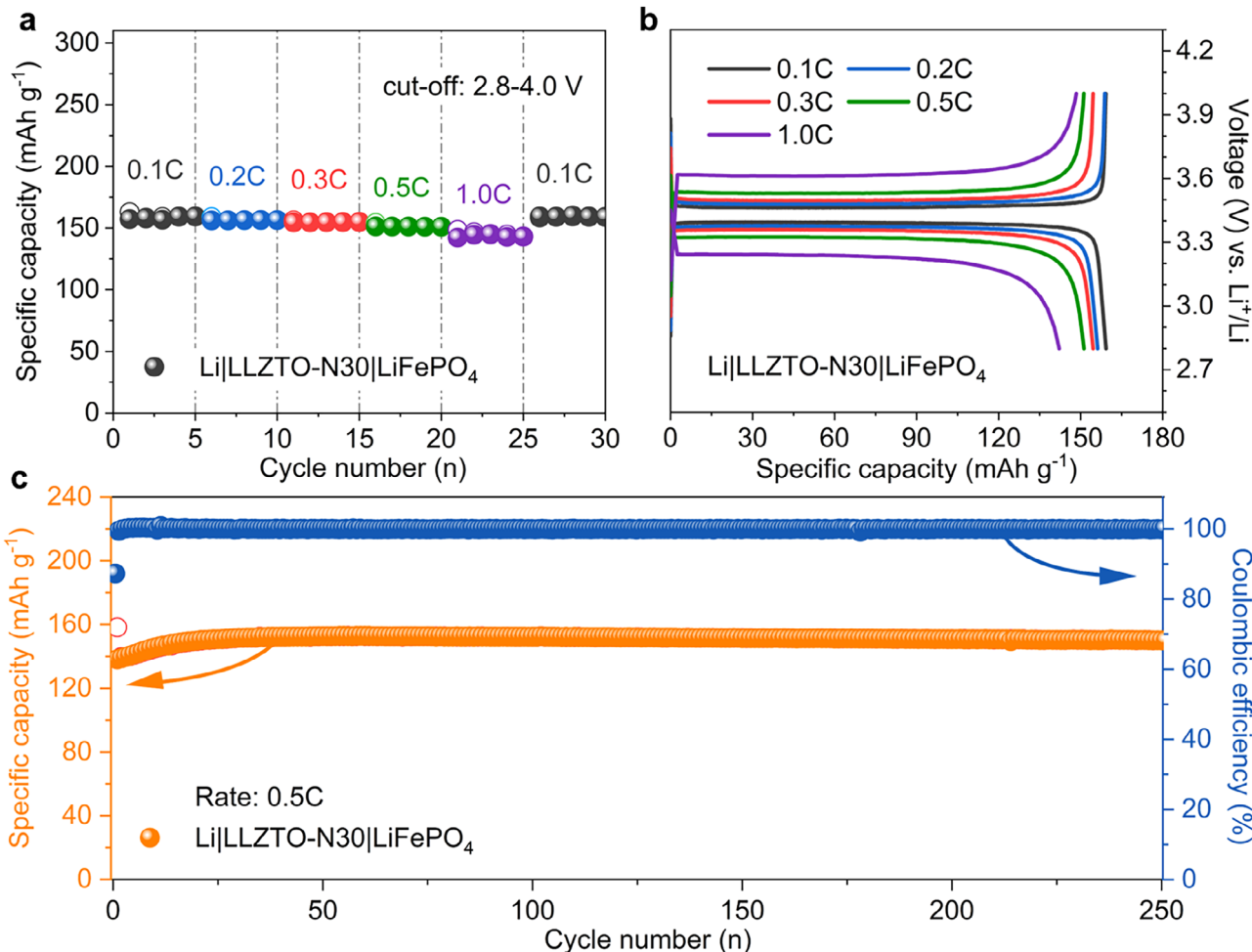


Figure 5. Rate performance (a), and corresponding charge/discharge specific capacity-voltage profiles (b) of Li|LLZTO-N30|LiFePO₄ full cells at different charge/discharge rates from 0.1C to 1C. Cycling performance of Li|LLZTO-N30|LiFePO₄ full cells at 0.5C (c).

300 h (Figure 4d). Under higher areal capacity cycling conditions (2.0 mAh cm⁻² at 25 °C and 4.0 mAh cm⁻² at 65 °C), the Li|LLZTO-N30|Li cell still displays a stable and low overpotential for over 100 h, demonstrating successfully establishment of a tightly bonded Li-SSEs interface (Figure 4e,f).

To explore the origin of the robust interfacial bonding between lithium and LLZTO-N30 electrolyte, DFT calculation was performed to calculate the variation in interfacial work of adhesion (W_{ad}) when a Li₂O-Li₃N hybrid interlayer is introduced (Figure 4g-l). W_{ad} , which is defined as the work required to separate two phases from each other, is used for assessing the interface bonding strength, and a higher W_{ad} typically indicates greater stability and tighter bonding of the interface.^[41] Notably, Li₂CO₃ shows a negative W_{ad} of -0.291 J m⁻², which makes it prone to detaching with lithium metal during cycling. Since Li₂O and Li₃N possess a high W_{ad} with both garnet ($W_{ad} = 1.590$ and 0.272 J m⁻²) and Li ($W_{ad} = 0.093$ and 0.192 J m⁻²), the constructed Li₂O-Li₃N interlayer functions as an effective adhesive to tightly bond the lithium anode and LLZTO. The good adhesion between the hybrid interlayer and both the lithium and LLZTO ensures a robust Li-SSEs interface, which is dynamically stable without

void formation even during a deep lithium stripping process (Figure 4m).

LLZTO with HNO₃ etching on one side for 30 s was assembled into full cells using LiFePO₄ as the cathode and Li metal as the anode to assess the practicality of HNO₃ treatment. An acceptable total interfacial impedance of ≈ 330 Ω cm² is observed for the assembled Li|LLZTO-N30|LiFePO₄ full cell at room temperature (Figure S18, Supporting Information). The assembled full cell delivers a high capacity of 158.3, 156.6, 154.9, 151.3, and 142.9 mAh g⁻¹, with acceptable electrode polarization at 0.1C, 0.2C, 0.3C, 0.5C, and 1.0C (1.0C ≈ 0.57 mA cm⁻²), respectively, indicating facilitated electrode reaction kinetics, which is attributed to the fast interfacial charge transfer (Figure 5a,b). When the current density was restored to 0.1C, the full cell delivers a reversible discharge capacity of 158.2 mAh g⁻¹, demonstrating the outstanding stability of the electrode structure and the interfacial connection. In addition, the Li|LLZTO-N30|LiFePO₄ cell shows excellent long-term stability and delivers a discharge capacity of 150.1 mAh g⁻¹ with a coulombic efficiency close to 100% after 250 charge-discharge cycles at 0.5C (0.5C ≈ 0.28 mA cm⁻², Figure 5c). The outstanding long-term stability of the full cell indicates that the Li₂O-Li₃N hybrid interlayer realizes a stable and

fast interfacial lithium-ion conduction, which is consistent with the electrochemical behaviors of the lithium symmetric cells.

3. Conclusion

In summary, a multifunctional hybrid intermediate interlayer was constructed at the Li/Garnet interface by a facile and efficient one-step surface etching method. Nitric acid was used to convert the Li_2CO_3 passivation layer on the LLZTO surface into a LiNO_3 lithiophilic layer. The spontaneous reaction between the LiNO_3 layer and Li not only promotes the interfacial contact through reactive wetting, but also in situ forms a $\text{Li}_2\text{O}-\text{Li}_3\text{N}$ hybrid Li^+ -conductive, while an electron-insulative interlayer less than 1 μm . In addition, the introduction of $\text{Li}_2\text{O}-\text{Li}_3\text{N}$ interlayer significantly improves the interfacial adhesion between LLZTO and Li anode, thus suppressing lithium-dendrite propagation and interfacial voids formation during the deep lithium stripping process. As a result, the fabricated $\text{Li}|\text{LLZTO-N30}|\text{Li}$ symmetric cell delivers a high critical current density of 2.6 mA cm^{-2} and a stable cycling performance for over 1000 h at 0.3 mA cm^{-2} . More impressively, benefitting from the strengthened interfacial adhesion, stable galvanostatic cycling of a symmetric cell for over 100 h without interfacial cavity formation at an ultra-high area-specific capacity of 4.0 mAh cm^{-2} is achieved. The $\text{Li}|\text{LLZTO-N30}|\text{LiFePO}_4$ full cell exhibits excellent rate performances (142.9 mAh g^{-1} at 1C) and outstanding long-term cycling stability (over 250 cycles at 0.5C). This facile and applicable strategy holds great promise for promoting the practical implementation of dendrite-free SSLMBs with high areal capacity.

Supporting Information

Supporting Information is available from the Wiley Online Library or from the author.

Acknowledgements

J.L. and X.M. contributed equally to this work. This work was supported by the National Natural Science Foundation of China (U23B20171) and the National Key R&D Program of China (2023YFE0119500).

Conflict of Interest

The authors declare no conflict of interest.

Data Availability Statement

Research data are not shared.

Keywords

dendrite suppressing, garnet-type solid-state electrolyte, high areal capacity cycling, multifunctional hybrid interlayer, work of adhesion

Received: May 22, 2025

Revised: July 13, 2025

Published online:

- [1] T. M. Gür, *Energy Environ. Sci.* **2018**, *11*, 2696.
- [2] P. Bonnick, J. Muldoon, *Energy Environ. Sci.* **2022**, *15*, 1840.
- [3] J. Li, H. Su, Y. Liu, Y. Zhong, X. Wang, J. Tu, *Electrochim. Energy Rev.* **2024**, *7*, 18.
- [4] J. Huang, C. Li, D. Jiang, J. Gao, L. Cheng, G. Li, H. Luo, Z. L. Xu, D. M. Shin, Y. Wang, Y. Lu, Y. Kim, *Adv. Funct. Mater.* **2024**, *35*, 241173.
- [5] J. Janek, W. G. Zeier, *Nat. Energy* **2023**, *8*, 230.
- [6] C. Wang, K. Fu, S. P. Kammampata, D. W. McOwen, A. J. Samson, L. Zhang, G. T. Hitz, A. M. Nolan, E. D. Wachsman, Y. Mo, V. Thangadurai, L. Hu, *Chem. Rev.* **2020**, *120*, 4257.
- [7] E. J. Cheng, H. Duan, M. J. Wang, E. Kazyak, H. Munakata, R. Garcia-Mendez, B. Gao, H. Huo, T. Zhang, F. Chen, R. Inada, K. Miyazaki, S. Ohno, H. Kato, S.-i. Orimo, V. Thangadurai, T. Abe, K. Kanamura, *Energy Storage Mater.* **2025**, *75*, 103970.
- [8] W. Feng, Y. Zhao, Y. Xia, *Adv. Mater.* **2024**, *36*, 2306111.
- [9] K. Yoon, S. Lee, K. Oh, K. Kang, *Adv. Mater.* **2021**, *34*, 2104666.
- [10] S. Kalnaus, N. J. Dudney, A. S. Westover, E. Herbert, S. Hackney, *Science* **2023**, *381*, abg5998.
- [11] V. Raj, V. Venturi, V. R. Kankanallu, B. Kuiri, V. Viswanathan, N. P. B. Aetukuri, *Nat. Mater.* **2022**, *21*, 1050.
- [12] C. D. Fincher, C. E. Athanasiou, C. Gilgenbach, M. Wang, B. W. Sheldon, W. C. Carter, Y.-M. Chiang, *Joule* **2022**, *6*, 2794.
- [13] J. Kasemchainan, S. Zekoll, D. Spencer Jolly, Z. Ning, G. O. Hartley, J. Marrow, P. G. Bruce, *Nat. Mater.* **2019**, *18*, 1105.
- [14] M. J. Wang, R. Choudhury, J. Sakamoto, *Joule* **2019**, *3*, 2165.
- [15] K. Lee, E. Kazyak, M. J. Wang, N. P. Dasgupta, J. Sakamoto, *Joule* **2022**, *6*, 2547.
- [16] C. Zhu, T. Fuchs, S. A. L. Weber, F. H. Richter, G. Glasser, F. Weber, H.-J. Butt, J. Janek, R. Berger, *Nat. Commun.* **2023**, *14*, 1300.
- [17] J.-S. Kim, G. Yoon, S. Kim, S. Sugata, N. Yashiro, S. Suzuki, M.-J. Lee, R. Kim, M. Badding, Z. Song, J. Chang, D. Im, *Nat. Commun.* **2023**, *14*, 782.
- [18] J. Biao, B. Han, Y. Cao, Q. Li, G. Zhong, J. Ma, L. Chen, K. Yang, J. Mi, Y. Deng, M. Liu, W. Lv, F. Kang, Y. B. He, *Adv. Mater.* **2023**, *35*, 2208951.
- [19] G. Lu, M. Li, P. Chen, W. Zheng, Z. Yang, R. Wang, C. Xu, *Energy Environ. Sci.* **2023**, *16*, 1049.
- [20] B.-Q. Xiong, Q. Nian, X. Zhao, Y. Chen, Y. Li, J. Jiang, S. Jiao, X. Zhan, X. Ren, *ACS Energy Lett.* **2022**, *8*, 537.
- [21] T. Wang, J. Duan, B. Zhang, W. Luo, X. Ji, H. Xu, Y. Huang, L. Huang, Z. Song, J. Wen, C. Wang, Y. Huang, J. B. Goodenough, *Energy Environ. Sci.* **2022**, *15*, 1325.
- [22] F. Han, A. S. Westover, J. Yue, X. Fan, F. Wang, M. Chi, D. N. Leonard, N. J. Dudney, H. Wang, C. Wang, *Nat. Energy* **2019**, *4*, 187.
- [23] X. Liu, R. Garcia-Mendez, A. R. Lupini, Y. Cheng, Z. D. Hood, F. Han, A. Sharafi, J. C. Idrobo, N. J. Dudney, C. Wang, C. Ma, J. Sakamoto, M. Chi, *Nat. Mater.* **2021**, *20*, 1485.
- [24] C.-L. Tsai, V. Roddatis, C. V. Chandran, Q. Ma, S. Uhlenbruck, M. Bram, P. Heitjans, O. Guillou, *ACS Appl. Mater. Interfaces* **2016**, *8*, 10617.
- [25] H. Huo, Y. Chen, N. Zhao, X. Lin, J. Luo, X. Yang, Y. Liu, X. Guo, X. Sun, *Nano Energy* **2019**, *61*, 119.
- [26] W. Feng, X. Dong, P. Li, Y. Wang, Y. Xia, *J. Power Sources* **2019**, *419*, 91.
- [27] M. He, Z. Cui, C. Chen, Y. Li, X. Guo, *J. Mater. Chem. A* **2018**, *6*, 11463.
- [28] A. C. Thenuwara, S. Narayan, E. L. Thompson, M. A. Quesada, T. F. Malkowski, K. D. Parrotte, K. E. Lostracco, L. A. Seeley, M. R. Borges, Z. Song, A. Rezizyan, M. Labant, X. Wu, M. E. Badding, K. G. Gallagher, *ACS Energy Lett.* **2024**, *9*, 2401.
- [29] S. Zhang, G. Yang, Z. Liu, S. Weng, X. Li, X. Wang, Y. Gao, Z. Wang, L. Chen, *ACS Energy Lett.* **2021**, *6*, 4118.
- [30] Z. Bi, R. Shi, X. Liu, K. Liu, M. Jia, X. Guo, *Adv. Funct. Mater.* **2023**, *33*, 202307701.

- [31] X. Bai, G. Zhao, G. Yang, M. Wang, J. Zhang, N. Zhang, *Energy Storage Mater.* **2023**, *63*, 103041.
- [32] G. Zhao, C. Luo, Q. Hua, *J. Mater. Chem. A* **2023**, *11*, 20174.
- [33] S. G. Yoon, B. S. Vishnugopi, D. L. Nelson, A. X. B. Yong, Y. Wang, S. E. Sandoval, T. A. Thomas, K. A. Cavallaro, P. Shevchenko, E. P. Alsaç, *Science* **2025**, *388*, 1062.
- [34] S. G. Yoon, B. S. Vishnugopi, E. P. Alsaç, W. J. Jeong, S. E. Sandoval, D. L. Nelson, A. Ayyaswamy, P. P. Mukherjee, M. T. McDowell, *ACS Nano* **2024**, *18*, 20792.
- [35] Y. Wang, C.-F. Lin, J. Rao, K. Gaskell, G. Rubloff, S. B. Lee, *ACS Appl. Mater. Interfaces* **2018**, *10*, 24554.
- [36] W. Qi, L. Ben, H. Yu, W. Zhao, G. Zhao, X. Huang, *Prog. Nat. Sci.: Mater. Int.* **2020**, *30*, 321.
- [37] J. Mizusaki, H. Tagawa, K. Saito, K. Uchida, M. Tezuka, *Solid State Ionics* **1992**, *53*, 791.
- [38] S. Lorger, R. Usiskin, J. Maier, *J. Electrochem. Soc.* **2019**, *166*, A2215.
- [39] W. Li, G. Wu, C. M. Araújo, R. H. Scheicher, A. Blomqvist, R. Ahuja, Z. Xiong, Y. Feng, P. Chen, *Energy Environ. Sci.* **2010**, *3*, 1524.
- [40] H.-K. Tian, Z. Liu, Y. Ji, L.-Q. Chen, Y. Qi, *Chem. Mater.* **2019**, *31*, 7351.
- [41] N. Jin, Y. Yang, X. Luo, J. Li, B. Huang, S. Liu, Z. Xiao, *Appl. Surf. Sci.* **2014**, *314*, 896.